Principal Role of Contact-Force Distribution in Determining the Thermal Conductivity of Supported Graphene

Yongjin Lee, Alexander J. Pak, Eunsu Paek, and Gyeong S. Hwang*

McKetta Department of Chemical Engineering, University of Texas, Austin, Texas 78712, USA

(Received 2 February 2015; revised manuscript received 4 March 2015; published 16 July 2015)

The thermal conductivity (κ) of graphene dramatically decreases once supported on a substrate, hindering its use for thermal management. To clarify the underlying mechanisms, we investigate the κ of graphene on amorphous SiO_2 by using molecular dynamics with particular attention to the graphene-substrate topography. Our analysis reveals that the suppression in κ increases with the nonuniformity of the forces acting on graphene, which tends to increase as the substrate-surface roughness and graphene conformity increase. Our findings highlight the importance of the interfacial morphology on κ and can provide guidance on the design of substrates to improve thermal transport through graphene.

DOI: 10.1103/PhysRevApplied.4.014006

I. INTRODUCTION

Current state-of-the-art techniques demonstrate that the thermal conductivity (κ) of freestanding graphene can be as large as 1500–5000 $Wm^{-1}K^{-1}$ [1–5], an order of magnitude larger κ than copper, but is reduced to around 600 $Wm^{-1}K^{-1}$ when supported on amorphous SiO_2 (a-SiO_2) at room temperature [6]. Yet, while it is well known that the κ of graphene is suppressed when supported on a substrate, the underlying mechanisms remain a subject of contention. Such an understanding will be critical to fully utilize graphene for thermal management of electronics [1].

In general, it is thought that κ is principally influenced by the strength of the van der Waals (vdW) coupling at the graphene-substrate interface. Several previous theoretical investigations suggest that the decrease in κ can be attributed to the dampening of the flexural acoustic (ZA) phonon modes which is tuned by the graphene-substrate interaction [7–9]. However, there is some debate as to whether the strengthening of the vdW coupling at the interface either enhances [9] or diminishes [7] thermal transport.

Beyond the vdW coupling strength, it could be important to consider additional factors that vary according to the morphological differences at the graphene-substrate interface. As depicted in Fig. 1, the topography of graphene may evolve due to contributions from internal and external forces. For instance, greater conformity can result from larger vdW interaction (i.e., more contact area), which can yield larger internal strain (i.e., more corrugation) depending on the surface roughness of the underlying substrate. As such, one possible source of the previously reported inconsistencies [7,9] could stem from the study of dissimilar graphene-substrate morphologies. We therefore postulate that the key to understanding the nature of phonon scattering at the interface could lie in the careful portrayal of the relationship between the interfacial topography and κ.

In this manuscript, the variation in κ of supported graphene is comprehensively studied by using classical molecular dynamics (MD) with variable SiO_2 surface roughness and graphene conformity. With particular attention to the interfacial energetics and forces, our analysis reveals that κ reduction scales directly with the nonuniformity of the forces acting on graphene, which we highlight as the "local dampening disorder." These findings underscore the importance of the careful characterization of substrate-surface conditions and may prove useful in superior control over thermal transport through low-dimensional materials supported on a substrate (or embedded in matrices of dissimilar materials).

II. COMPUTATIONAL METHODS

Graphene/a-SiO_2 *sample preparation.*—Four defect-free a-SiO_2 slabs are constructed by using continuous random network Metropolis Monte Carlo (CRN-MMC) simulations following the method described in Ref. [10]; each slab contains 3600 SiO_2 units with a lateral thickness of 7.77×7.98 nm^2, yielding a slab thickness of around 2 nm. A single graphene sheet is then placed on the top and bottom surfaces of the a-SiO_2 slab. The graphene/a-SiO_2 structures are relaxed by using MD under periodic boundary conditions by the LAMMPS package [11]. For each system, we consider the nonconformed cases, which are composed of 18×32 rectangular supercells (2304 atoms), and the optimally conformed configurations of graphene, which are determined by varying its lateral size up to a 19×33 rectangular supercell (2508 atoms) as described in Supplemental Material and Table S1 [12]. The C-C

*To whom all correspondence should be addressed.
gshwang@che.utexas.edu

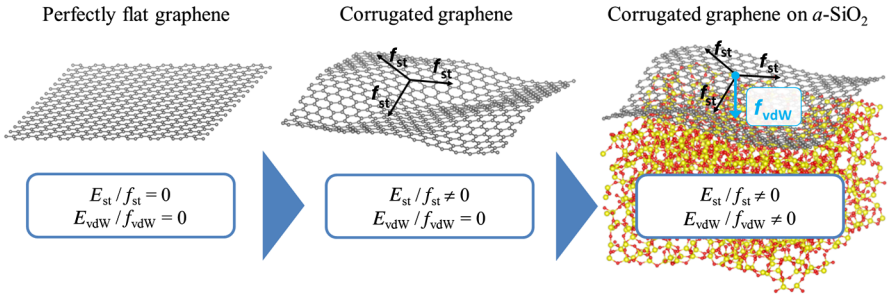

FIG. 1. Schematic demonstrating the evolution of the topography of graphene due to internal and external forces. Thermal perturbation of perfectly flat graphene induces local internal strain and thereby yields corrugated graphene; the internal strain can be described by the strain energy (E_{st}) and strain force (f_{st}). The presence of a substrate introduces vdW interactions at the interface which further influence the graphene morphology; the vdW coupling can be described by the vdW energy (E_{vdW}) and vdW force (f_{vdW}). The gray sheet represents graphene, while the yellow and red balls represent Si and O atoms, respectively, in amorphous SiO_2 (a-SiO_2).

interactions are described by an optimized Tersoff potential [4]. Additional simulation details, including the Si-O potential and C-Si and C-O Lennard-Jones parameters, can be found in Ref. [10].

Thermal conductivity of freestanding graphene.—To estimate reliable values for κ at 300 K, we calculate the κ for freestanding graphene with four different lengths ($L = 62.1$, 124.3, 248.7, and 373.0 nm) and width 7.97 nm corresponding to a $(144, 288, 576, 864) \times 32$ rectangular supercell; periodic boundary conditions are employed in all three directions with 10 nm of vacuum space included in the vertical direction to remove interactions with the periodic image. The κ at infinite length is then extrapolated from $1/L$ vs $1/\kappa$ [13] in which the thickness of graphene is assumed to be 0.335 nm; such a treatment is necessary, as the phonon mean-free path of graphene is estimated to be approximately 775 nm, which is much larger than the simulation domain [1]. To obtain the κ at each L, we perform ten independent reverse nonequilibrium MD (RNEMD) simulations [14] with different initial velocity distributions for statistical accuracy. Each system is equilibrated for 100 ps within the canonical (NVT) ensemble with a Nosé-Hoover thermostat [15] and followed by 1 ns within the microcanonical (NVE) ensemble while imposing a heat flux within graphene with a velocity swap interval of 50 fs; here, all MD simulations adopt a 0.5-fs time step. The temperature profile is extracted every 5 ps, and the κ is computed from the average gradient of the linear region of the profile between the heat source and sink. Since the Debye temperature of graphene is above 2000 K [16], we include the quantum correction factor according to the procedure shown in Ref. [17].

Thermal conductivity of graphene on α-quartz and a-SiO_2.–We use a similar approach to calculate the κ of supported graphene. Here, we replicate each graphene/a-SiO_2 and graphene/α-quartz sample to increase the length L to 62.1, 77.7, 93.2, and 124.3 nm and follow the same RNEMD methodology to calculate κ. In addition, the κ of the top and bottom graphene sheets are computed separately and considered independently.

III. RESULTS AND DISCUSSION

First, the κ of freestanding graphene at 300 K is calculated in order to establish a baseline for comparisons with supported graphene. Our predicted $\kappa = 2715 \pm 60$ $Wm^{-1}K^{-1}$ is within the range of values previously reported from both experiments and simulations (1500–5000 $Wm^{-1}K^{-1}$) [1–5]. The thermally induced corrugations of graphene, which are quantified based on the standard deviation of the equilibrium atomic height distribution ($\sigma_{z,gr}$), is found to be 0.8 Å at 300 K. However, we should point out that κ tends to decrease with increasing $\sigma_{z,gr}$, which follows from compressive strain [12], as demonstrated in Fig. 2; the sensitivity of κ to corrugation may be partially responsible for the scattered κ values reported in prior experiments [1–3]. As discussed below, $\sigma_{z,gr}$ can also vary as the substrate roughness ($\sigma_{z,sub}$) and the subsequent conformity of graphene change.

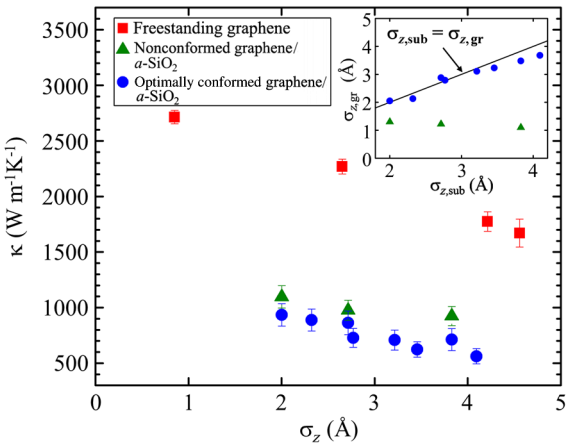

FIG. 2. Thermal conductivity (κ) as a function of surface roughness (σ_z); for freestanding graphene (red squares), σ_z refers to the corrugation of graphene ($\sigma_{z,gr}$), while for supported graphene (green triangles and blue circles), σ_z refers to the substrate surface roughness ($\sigma_{z,sub}$). The inset compares $\sigma_{z,gr}$ to that of $\sigma_{z,sub}$ for each supported graphene case; points far below the black diagonal line indicate poor conformity.

TABLE I. Calculated thermal conductivity (κ), strain to vdW energy ratio (E_{st}/E_{vdW}), and standard deviation or mean of the vdW and strain force per graphene atom [$\sigma(|f_{vdW,z}|)/\mu(|f_{vdW,z}|)$ and $\sigma(|f_{st}|)/\mu(|f_{st}|)$] for graphene supported on α-quartz and a-SiO_2 with the corresponding graphene ($\sigma_{z,gr}$) and substrate ($\sigma_{z,sub}$) roughness.

Model ($\sigma_{z,gr}/\sigma_{z,sub}$)	κ ($Wm^{-1}K^{-1}$)	E_{st}/E_{vdW} (eV nm^{-2})	$\sigma(\|f_{vdW,z}\|)/\mu(\|f_{vdW,z}\|)$ (eV $Å^{-1}$)	$\sigma(\|f_{st}\|)/\mu(\|f_{st}\|)$ (eV $Å^{-1}$)
Graphene/quartz (0.14/0.00)	1642 ± 102	0.6514/0.0311	0.0016/0.0126	0.0093/0.0214
Nonconformed graphene/a-SiO_2 (1.1/3.8)	923 ± 86	0.6231/0.1833	0.0252/0.0114	0.0159/0.0243
Optimally conformed graphene/a-SiO_2 (3.4/3.8)	713 ± 99	1.3577/0.6973	0.0354/0.0274	0.0377/0.0331

Next, the κ of graphene on atomically smooth α-quartz (graphene/quartz) as compared to atomically rough a-SiO_2 are investigated; a Monte Carlo scheme [10] is used to generate an a-SiO_2 slab with $\sigma_{z,sub} = 3.8$ Å. In addition, we consider the two scenarios when graphene is nonconformed (nonconformed graphene/a-SiO_2) and optimally conformed (optimally conformed graphene/a-SiO_2) to a-SiO_2, the latter of which is obtained after graphene is compressed biaxially by around 5% (3%) in the x (y) direction. As seen in Table I, the predicted κ of the optimally conformed graphene/a-SiO_2 case is found to be 713 ± 99 $Wm^{-1}K^{-1}$, a dramatic decrease of nearly 75% from that of freestanding graphene, which is reasonably close to experimentally measured values [6]. On the other hand, the suppression is greatly mitigated in the graphene/quartz case ($\kappa = 1642 \pm 86$ $Wm^{-1}K^{-1}$).

Comparing the aforementioned three cases, the κ reduction of graphene is observed to increase with the following trend: graphene/quartz < nonconformed graphene/a-SiO_2 < optimally conformed graphene/a-SiO_2. A few interesting features can be found from an analysis of the interfacial energetics and forces, which are summarized in Table I. First, note that the vdW interaction energy (E_{vdW}) is comparable in the graphene/quartz and nonconformed graphene/a-SiO_2 cases, although κ significantly decreases by around 700 $Wm^{-1}K^{-1}$. On the other hand, the internal strain energy (E_{st}) exhibits a noticeable increase due to the increasing $\sigma_{z,gr}$ that follows from the partial conformity of graphene to the rough surface of a-SiO_2.

Looking beyond the energetics, a substantial increase in the standard deviation of the vdW force [$\sigma(|f_{vdW,z}|)$] [18] and internal strain force [$\sigma(|f_{st}|)$] is predicted in the nonconformed graphene/a-SiO_2 case as compared to the graphene/quartz case. Meanwhile, the mean magnitude of the vdW force [$\mu(|f_{vdW,z}|)$] and strain force [$\mu(|f_{st}|)$] expectedly exhibit trends similar to the E_{vdW} and E_{st}, respectively. These results clearly demonstrate that κ should not be determined solely by the strength of the vdW coupling but also by the uniformity of forces (that depends upon the graphene-substrate morphology), herein called the local dampening disorder.

A comparison of the optimally conformed graphene/a-SiO_2 case to the nonconformed graphene/a-SiO_2 case further reveals that both $E_{vdW/st}$ and $\sigma(|f_{vdW,z/st}|)$ tend to increase with κ reduction, which supports that κ is not directly related to the magnitude of E_{vdW}. To examine the relationship between κ and the local dampening disorder in depth, we perform subsequent calculations for nonconformed graphene and optimally conformed graphene supported on a-SiO_2 substrates with varying $\sigma_{z,sub}$.

Figure 2 shows the predicted κ of graphene on a-SiO_2 as a function of $\sigma_{z,sub}$. As $\sigma_{z,sub}$ for different optimally conformed graphene/a-SiO_2 samples (blue circles) increases from 2.00 to 4.09 Å, the predicted κ tends to decrease from 935 ± 101 to 562 ± 68 $Wm^{-1}K^{-1}$, which is a reasonable range given the scattered values reported in both experiments [3,6] and simulations [19]. The κ of nonconformed graphene/a-SiO_2 (green triangles) is similarly repressed from 1096 ± 101 to 923 ± 86 $Wm^{-1}K^{-1}$, although to a lesser extent than the optimally conformed graphene/a-SiO_2 cases. When compared to freestanding graphene (red squares), it is evident that the presence of the substrate suppresses κ by more than a factor of 2. Furthermore, these results illustrate that the surface roughness of a-SiO_2 and the conformity of graphene can strongly influence κ; specifically, we find that κ decreases as $\sigma_{z,sub}$ increases and more so when graphene is well conformed to a-SiO_2.

We next examine the relationship between the local dampening disorder induced on supported graphene and κ in Fig. 3, in which the relative importance of $\sigma(|f_{vdW,z}|)$ and $\sigma(|f_{st}|)$ is considered. Figure 3 depicts $\sigma(|f_{vdW,z}|)$ and $\sigma(|f_{st}|)$ as a function of κ for both optimally conformed graphene/a-SiO_2 and nonconformed graphene/a-SiO_2. Remarkably, we observe that the decrease in κ distinctly follows an increase in both $\sigma(|f_{vdW,z}|)$ and $\sigma(|f_{st}|)$, although the dependence on $\sigma(|f_{vdW,z}|)$ seemingly dominates in these cases; on the other hand, κ is revealed to be insensitive to both $\mu(|f_{vdW,z}|)/\mu(|f_{st}|)$ and E_{vdW}/E_{st} [12]. Recall that the optimal conformation of graphene tends to be less coarse than the underlying substrate surface [10], which can result in irregularities in the contact-force distribution while the strain-force distribution is comparatively smoother. However, we may conceive a situation in which graphene and the underlying substrate are corrugated with uniform separation, in which

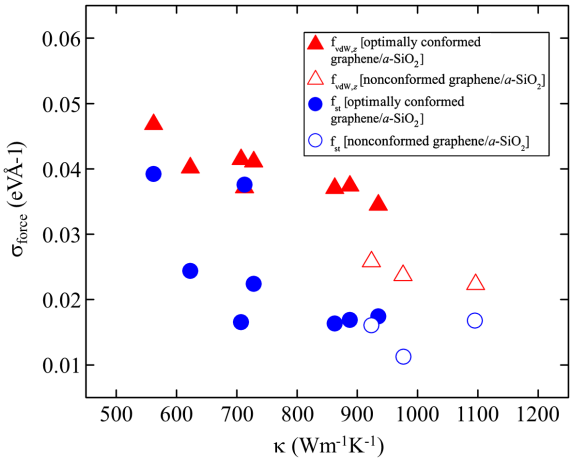

FIG. 3. Relationship between the standard deviation of the applied vdW and strain force (σ_{force}) and the thermal conductivity (κ).

case it is possible that $\sigma(|f_{\text{st}}|)$ is comparatively larger than $\sigma(|f_{\text{vdW},z}|)$. Nonetheless, these results demonstrate that, when graphene is supported on a substrate, κ strongly depends on the degree of uniformity of the force distribution along the graphene sheet, which in turn suggest that the broad range of experimental values for the κ of supported graphene may be attributed to differences in the morphology of the graphene-substrate interface.

An analysis of the spatially resolved vibrational eigenmodes (λ) can further reveal the nature of κ suppression in the presence of different substrate or conformity conditions. The phonon participation ratio [20] (p_λ) for each λ is first calculated for the three cases (of graphene/quartz, nonconformed graphene/a-SiO_2, and optimally conformed graphene/a-SiO_2 from Table 1) as follows:

$$p_\lambda = N\sum_i \left(\sum_{j=x,y,z} \epsilon^*_{ij,\lambda}\epsilon_{ij,\lambda} \right)^2,$$

where $\epsilon_{ij,\lambda}$ is the vibrational eigenvector component for atom i in direction j over all atoms N; p_λ corresponds to the fraction of atoms participating in the λth mode and varies between unity and zero for completely delocalized and localized phonon states, respectively. We find that the calculated suppression in κ, which varies as graphene/quartz < nonconformed graphene/a-SiO_2 < optimally conformed graphene/a-SiO_2, coincides with the apparent localization of low-energy acoustic (<400 cm^{-1}) and high-energy optical (>1200 cm^{-1}) phonon modes [12].

The fractional distribution (per atom) of localized λ (denoted as $\Phi_{ij,\Gamma}$) within the range $\Gamma = \{\lambda\colon\ p_\lambda < 0.3\}$ can be computed from [21]

$$\Phi_{ij,\Gamma} = \frac{\sum_{\lambda\in\Gamma} \epsilon^*_{ij,\lambda}\epsilon_{ij,\lambda}}{\sum_{i'}\sum_{\lambda\in\Gamma} \epsilon^*_{i'j,\lambda}\epsilon_{i'j,\lambda}}$$

and indicates the relative concentration (or contribution) of atom i to the λ modes in Γ. The $\Phi_{ij,\Gamma}$ ($j = z$) throughout the graphene lattice is depicted in Figs. 4(a)–4(c). It is evident that in the graphene/quartz case [Fig. 4(a)] $\Phi_{ij,\Gamma}$ is uniformly distributed across the lattice, showing that all atoms are nearly equally involved as an extended mode; according to our previous analysis, this is related to the flat and homogeneous nature of the graphene-substrate topography, as depicted by a color map of the spatially

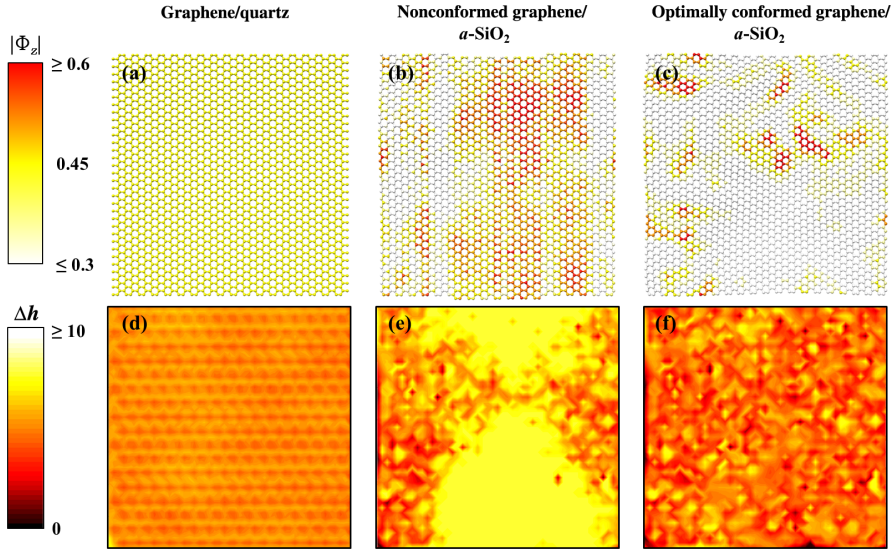

FIG. 4. Spatial distribution of eigenmodes with phonon participation ratio <0.3 ($|\Phi_z|$) for the (a) graphe/quartz, (b) nonconformed graphene/a-SiO_2, and (c) optimally conformed graphene/a-SiO_2 cases. Color maps of the spatially resolved distance between graphene and the substrate for the (d) graphene/quartz, (e) nonconformed graphene/a-SiO_2, and (f) optimally conformed graphene/a-SiO_2 cases.

resolved distance between graphene and the substrate in Fig. 4(d). The nonconformed graphene/a-SiO_2 case [Fig. 4(b)] contrastingly displays a distinct discontinuity in which the central atoms [dark yellow to red] are seen to contribute significantly more to these phonon modes than the outer atoms [light yellow to white] and indicate a clear departure from an extended state. The corresponding separation distance color map [Fig. 4(e)] demonstrates that these regions with localized modes are confined by the contact between graphene and the substrate surrounding a void space due to poor conformation; we note, however, that these modes remain fairly diffuse over the pocket region likely due to the smoothness of the local contact-force distribution. In the optimally conformed graphene/a-SiO_2 case [Fig. 4(c)], the majority contributors to the λ modes in Γ are further confined spatially (i.e., hot spots). As the conformity between graphene and a-SiO_2 is increased, the length scale of morphological mismatch subsequently becomes smaller (i.e., sharper and more confined regions of mismatch can occur) [Fig. 4(f)] and can contribute to the formation of these so-called hot spots. We can therefore hypothesize that the local variance (and, specifically, the frequency) of the vdW interaction acting on graphene, which is driven by these morphological differences, serves as a type of disorder that localizes vibrational eigenstates and correspondingly suppresses thermal transport and κ.

IV. CONCLUSIONS

In summary, we demonstrate the importance of the local dampening disorder induced by morphological differences on the suppression of thermal transport in supported graphene. The thermal conductivity of supported graphene is found to be sensitive to both the a-SiO_2 substrate-surface roughness and graphene conformity with modulation within 500 $Wm^{-1}K^{-1}$. Our analysis attributes this suppression to increasing nonuniformity of the contact-force distribution, which is also independent of the van der Waals coupling strength and internal strain energy. These findings suggest that the thermal conductivity of graphene (and other low-dimensional materials) can be influenced by factors such as lattice mismatch, isotope or chemical doping, or surface functionalization by affecting the uniformity of the force distribution, which will require careful consideration in the future.

ACKNOWLEDGMENTS

This work is supported in part by the National Science Foundation (CBET-0933557), the Robert A. Welch Foundation (F-1535), and the NSF-NASCENT Engineering Research Center (Cooperative Agreement No. EEC-1160494). Y. L. is grateful for the scholarship from the Donald D. Harrington Fellows Program. We also thank the Texas Advanced Computing Center for the use of their computing resources.

Y. L. and A. J. P. contributed equally to this work.

[1] S. Ghosh, I. Calizo, D. Teweldebrhan, E. P. Pokatilov, D. L. Nika, A. A. Balandin, W. Bao, F. Miao, and C. N. Lau, Extremely high thermal conductivity of graphene: Prospects for thermal management applications in nanoelectronic circuits, Appl. Phys. Lett. **92**, 151911 (2008).

[2] X. Xu, L. F. C. Pereira, Y. Wang, J. Wu, K. Zhang, X. Zhao, S. Bae, C. Tinh Bui, R. Xie, J. T. L. Thong, B. H. Hong, K. P. Loh, D. Donadio, B. Li, and B. Özyilmaz, Length-dependent thermal conductivity in suspended single-layer graphene, Nat. Commun. **5**, 3689 (2014).

[3] W. Cai, A. L. Moore, Y. Zhu, X. Li, S. Chen, L. Shi, and R. S. Ruoff, Thermal transport in suspended and supported monolayer graphene grown by chemical vapor deposition, Nano Lett. **10**, 1645 (2010).

[4] L. Lindsay and D. A. Broido, Optimized Tersoff and Brenner empirical potential parameters for lattice dynamics and phonon thermal transport in carbon nanotubes and graphene, Phys. Rev. B **81**, 205441 (2010).

[5] B. Kong, S. Paul, M. Nardelli, and K. Kim, First-principles analysis of lattice thermal conductivity in monolayer and bilayer graphene, Phys. Rev. B **80**, 033406 (2009).

[6] J. H. Seol, I. Jo, A. L. Moore, L. Lindsay, Z. H. Aitken, M. T. Pettes, X. Li, Z. Yao, R. Huang, D. Broido, N. Mingo, R. S. Ruoff, and L. Shi, Two-dimensional phonon transport in supported graphene, Science **328**, 213 (2010).

[7] B. Qiu and X. Ruan, Reduction of spectral phonon relaxation times from suspended to supported graphene, Appl. Phys. Lett. **100**, 193101 (2012).

[8] D. Singh, J. Murthy, and T. Fisher, Mechanism of thermal conductivity reduction in few-layer graphene, J. Appl. Phys. **110**, 044317 (2011).

[9] Z.-Y. Ong and E. Pop, Effect of substrate modes on thermal transport in supported graphene, Phys. Rev. B **84**, 075471 (2011).

[10] E. Paek and G. S. Hwang, A computational analysis of graphene adhesion on amorphous silica, J. Appl. Phys. **113**, 164901 (2013).

[11] S. Plimpton, Fast parallel algorithms for short-range molecular dynamics, J. Comput. Phys. **117**, 1 (1995).

[12] See Supplemental Material at http://link.aps.org/supplemental/10.1103/PhysRevApplied.4.014006 for additional details on the optimal conformation of graphene, the relationship between graphene corrugation and applied strain, the impact of energetics and forces on thermal conductivity, and phonon participation ratios.

[13] P. K. Schelling, S. R. Phillpot, and P. Keblinski, Comparison of atomic-level simulation methods for computing thermal conductivity, Phys. Rev. B **65**, 144306 (2002).

[14] F. Müller-Plathe, A simple nonequilibrium molecular dynamics method for calculating the thermal conductivity, J. Chem. Phys. **106**, 6082 (1997).

[15] W. Hoover, Canonical dynamics: Equilibrium phase-space distributions, Phys. Rev. A **31**, 1695 (1985).

[16] D. K. Efetov and P. Kim, Controlling Electron-Phonon Interactions in Graphene at Ultrahigh Carrier Densities, Phys. Rev. Lett. **105**, 256805 (2010).

[17] J.-W. Jiang, J. Lan, J.-S. Wang, and B. Li, Isotopic effects on the thermal conductivity of graphene nanoribbons: Localization mechanism, J. Appl. Phys. **107**, 054314 (2010).

[18] Here, we report only the vertical component of the vdW force for clarity, which contributes more than 90% to the total force.

[19] J. Chen, G. Zhang, and B. Li, Substrate coupling suppresses size dependence of thermal conductivity in supported graphene, Nanoscale **5**, 532 (2013).

[20] A. Bodapati, P. Schelling, S. Phillpot, and P. Keblinski, Vibrations and thermal transport in nanocrystalline silicon, Phys. Rev. B **74**, 245207 (2006).

[21] Y. Wang, B. Qiu, and X. Ruan, Edge effect on thermal transport in graphene nanoribbons: A phonon localization mechanism beyond edge roughness scattering, Appl. Phys. Lett. **101**, 013101 (2012).